

Cobalt–Nickel Exchange in Exfoliated Battery Layered Cathode Sheets with Application to Recycling

Kevin Leung,* Clare Davis-Wheeler Chin, and Candace K. Chan

With the emerging dominance of electric vehicles (EV) in the transportation sector, recycling or upcycling spent battery materials will be required to reduce EV costs, lessen waste, and ease critical material supply chain issues for EV batteries. Motivated by work in the literature describing the exfoliation of layered oxides, first-principles calculations are performed to show that Li_xCoO_2 , if exfoliated into nanosheets, can readily undergo transition metal cation exchange in aqueous media. The substitution of Co^{3+} or Co^{4+} cations inside the sheet by Ni^{2+} is associated with modest

reaction barriers ($\Delta G^* \approx 0.3\text{--}0.7 \text{ eV}$) and is at most mildly endothermic ($\Delta G \approx 0.2\text{--}0.3 \text{ eV}$). In contrast, previous battery degradation studies have shown that Co^{3+} diffusion is strongly inhibited inside bulk layered oxides. This suggests that processing spent layered oxides as nanosheets can provide a potentially low-energy-cost pathway to altering the transition metal and/or dopant stoichiometry, which can be used toward developing new room-temperature upcycling routes for cathodes from end-of-life batteries.

1. Introduction

Battery recycling and upcycling will help secure a domestic supply chain for battery materials and help lower electric vehicle (EV) costs.^[1–5] In terms of materials costs, the most valuable parts of EV batteries are the layered oxide cathode active materials, which contain not only lithium, but also cobalt and other transition metals. Current industrial-scale battery recycling processes rely on pyro- and hydrometallurgical methods, which use high-temperature and acid leaching processes, respectively, to break down the entire oxide and recover the metal contents.^[1–4] These processes tend to be energy intensive and/or produce significant waste products. Many direct recycling approaches reported recently describe strategies to replenish the lost lithium content and recover degraded crystal structures in spent battery materials.^[6–15] These methods drastically reduce the energy input needed to reuse spent battery cathode materials but do not change the transition metal stoichiometry in the cathode oxides unless further reactions with additional transition metal reagents are performed.^[16–20] This is an issue because the transition metal ratio in $\text{LiNi}_x\text{Mn}_y\text{Co}_z\text{O}_2$ (NMC), the cathode material used in >50% of EV battery cathodes worldwide as of 2023, is continually changing.^[21] Currently, NMC622 (60% Ni, 20% Mn, 20% Co)^[21]

and possibly NMC811 are supplanting NMC111 and NMC532 cathodes previously installed in EVs, while the older, Co-rich cathodes, including consumer electronics batteries that use LiCoO_2 (LCO), are reaching end of life. The reduction of Co content in lithium-ion batteries helps to lessen the reliance on a critical material element currently mined in conflict regions,^[22] while the increase of Ni content raises lithium utilization and the operating voltage, thus increasing the energy density.^[23] Finally, doping NMC with metals like Al^{3+} to further improve cycling properties is the subject of active research.^[24] Such dopants may be incorporated into future cathodes at industrial scales, making it important to include them in upcycling schemes. As a result, there is still room for basic science research into alternate recycling routes,^[6,7,25,26] particularly if the metal oxide composition can be altered in the process. Specifically, in the case of LCO or Co-rich NMCs, this means approaches to exchange the Co with Ni and other metal elements may allow for upcycling of the cathode materials and recovery of Co. Fundamental science studies can further lead to the design of future battery cathodes with built-in recycling pathways. Recycling of anode materials like graphite^[27] is also highly relevant, but this work will focus on transition metal oxide-based cathodes.

Monovalent metal ion exchange in oxides, and multivalent metal exchange in sulfides and selenides, have been amply demonstrated, especially in the nanoscience literature.^[28–30] In contrast, changing the divalent and multivalent cation content in oxides, which is desirable for battery upcycling, has seldom been reported at room temperature. (Henceforth we denote multivalent metal exchange between oxide and the liquid phase simply as “cation exchange.”) One notable exception is Fe^{2+} ion exchange in FeOOH ^[31–33]; however, the rate is low and the process is not complete over tens of hours.

To accelerate cation exchange or substitution, reducing the oxide dimensionality and increasing the surface area have been successfully demonstrated in oxide^[34] and layered double hydroxide^[35,36] nanosheets. This approach seems particularly

K. Leung
Sandia National Laboratories
Org. 8915
MS 0750, Albuquerque, NM 87185, USA
E-mail: kleung@sandia.gov

C. Davis-Wheeler Chin
MESA Microsystems Engineering, Science, and Applications
MS 1084, Albuquerque, NM 87185, USA

C. K. Chan
Materials Science & Engineering
School for Engineering of Matter, Transport and Energy
Arizona State University
Tempe, AZ 85272, USA

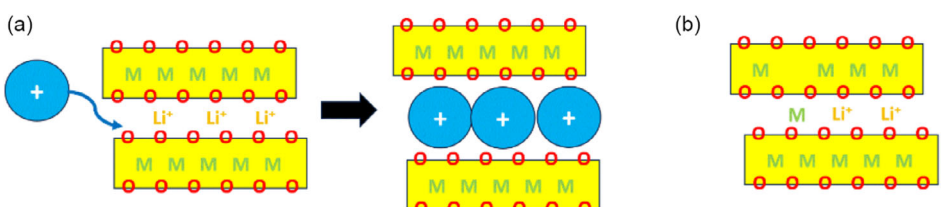


Figure 1. a) Schematic of bulky organic monovalent cations (blue spheres) displacing Li⁺ in the space between transition metal ("M") oxide sheets, facilitating exfoliation. b) Schematic of a precursor to the "dumbbell" defect formation; in 3D space both Li⁺ and M cations would be tetrahedrally coordinated between the sheets, while M would be octahedrally coordinated inside the oxide sheets.

attractive for LCO and NMC, which are made of sheets of edge-sharing transition metal oxide octahedra separated by layers of Li⁺ ions (Figure 1a). The oxide layers are held together by electrostatic forces exerted by the Li⁺ ions between them, which can be lessened via delithiation, a process that is coupled with oxidation of Co³⁺ in LCO or Ni²⁺/Co³⁺ in NMC. Inside bulk LCO or NMC oxides, a prerequisite to removal or exchange of the transition metals is their mobilization from the transition metal layer into the Li⁺ layer. Mobilizing Co³⁺ this way involves the formation of energetically unfavorable "dumbbell" defects with four-coordinated Co-cations (see Figure 1b, which depicts a precursor to the dumbbell defect).^[37] In fact, the stability of six-coordinated Co³⁺, arising from its electronic structure, may be a key reason for why Co has been needed in NMC and NCA compounds so far. If one were to exfoliate the bulk layered oxide into nanosheets, however, the Co cation can become coordinated to solvent molecules in addition to the oxygen anions on the sheet surface. Its charge state can also change spontaneously to Co²⁺, the state Co ions typically adopt when in solution, via electron transfer from the rest of the exfoliated sheet. We hypothesize that replacing Co in the nanosheets by metal cations dissolved in the solvent phase should occur far more readily in exfoliated sheets than in bulk NMC oxides. (See also ref.^[38] regarding transition metal ions extrusion from the basal surface of layered oxides.) After cation exchange, the exfoliated nanosheets can be reassembled into bulk cathode oxide materials via sintering.

Layered NMC oxide materials, and the structurally similar LCO, have indeed been successfully exfoliated using nanoscience processing methods in aqueous media.^[39–47] These methods generally rely on intercalation of bulky tetraalkylammonium cations into the Li-containing interlayers to force apart the metal oxide layers (typically with assistance from mechanical agitation and/or thermal energy), forming mono- and bilayer nanosheets.^[47] Delithiation, or removal of some interlayer Li⁺ via chemical or electrochemical methods, is a necessary pretreatment to increase electrostatic repulsion between the negatively charged metal oxide slabs and create interlayer vacancies that enable introduction of the bulky cations.^[41] The use of mildly alkaline media^[39,40] for exfoliation instead of the more usual acid treatment has made it possible to avoid potential acid-induced damage of the layered oxide structure. Relithiation and reassembly of the exfoliated nanosheets into working cathodes have also been demonstrated.^[39,40] However, cation exchange has not been part of the previous studies.

Here, we apply density functional theory (DFT) calculations to explore the energetics and kinetics involved in cation exchange

in Li_xCoO₂ and Li_xNiO₂ (LNO) nanosheets. These material choices represent the NMC compositions with the least and most amount of cation exchange when starting from LCO. As shown, our predictions are consistent with a low-energy pathway that was predicted in previous studies in connection with cathode degradation,^[48] wherein transition metal ions were found to preferentially diffuse through the basal plane to the surface of the top oxide layer. To some extent, we are leveraging our understanding of battery degradation studies in reverse to facilitate recycling,^[49] including DFT modeling studies of transition metal ion dissolution from oxide surfaces.^[48,50–52] In addition to static DFT barrier-binding calculations, more rigorous dynamic *ab initio* molecular dynamics (AIMD) free energy simulations are applied. Discussions of the results from experimental perspectives are given.

2. Experimental Section

Both static DFT calculations and dynamic AIMD simulations were conducted using the Vienna Atomic Simulation Package (VASP).^[53–56] The static and dynamic approaches were complementary, each emphasizing elements which corresponded to different themes of the experimental settings: presence of organic cations and of the aqueous environment, respectively. The Perdew–Burke–Ernzerhof (PBE) functional^[57] and the rotationally invariant DFT + U augmentation for transition metal 3d-orbitals^[58] were applied. The U–J parameters were 4.85, 3.30, and 5.95 eV for Mn, Co, and Ni, respectively, similar to those used in the literature.^[59] All simulation cells were charge neutral. The charge state of each transition metal ion was deduced from the local magnetic moment on that ion. No constraint was put on the total magnetic moment of the system, except during restart of AIMD trajectories (see below).

In static DFT calculations, Born–Oppenheimer energy convergence criterion of 10⁻⁴ eV and 2 × 2 sampling of the Brillouin zone were enforced. In AIMD simulations, the convergence criterion was 10⁻⁶ eV, the time step was 0.5 fs, the temperature was set at T = 400 K (using a Nose thermostat to accelerate sampling of water configurations because PBE predicts overstructured water at T = 300 K), and the Brillouin zone was sampled at the Γ-point only. In all cases, the energy cutoff was 400 eV, and dispersion correction, such as DFT-D2,^[60] was not included.^[61] The convergence of DFT Kohn–Sham orbitals during AIMD simulations can be challenging in these spin-polarized systems with

multiple transition metal ions; the preconditioned conjugate gradient method ("IALGO = 58" in VASP) was found to be more reliable than nominally faster options which may fail to converge Kohn-Sham orbitals in some atomic configurations.

The periodically replicated simulation cell has dimensions $15.19 \times 11.50 \times 24 \text{ \AA}^3$ in static DFT calculations, and the oxide sheet has a $\text{Li}_{10}\text{Co}_{24}\text{O}_{48}$ stoichiometry. We attempted to replace one Co (Co^{3+} or Co^{4+}) in the sheet with a single Ni^{2+} cation adsorbed on the oxide surface using climbing image nudged elastic band barrier-finding calculations.^[62] Five tetramethylammonium (TMA) monovalent ions were adsorbed onto each oxide surface to mimic the exfoliation additives used in previous experiments.^[39,40] Additionally, 2 OH^- ions and 2 H_2O molecules were added on each side, in position to form hydrogen-bonded chains that can bond to an Ni^{2+} adsorbed on, or Co cation extruded from, the oxide surfaces (Figure 2). The stoichiometry represented a slightly delithiated (oxidized) charge state, with an average formal charge of +3.33 for the 24 transition metal ions inside the sheet. The optimized atom configurations were most likely metastable, not global minima. Since we were interested in local configuration changes, we found this acceptable. However, as will be discussed, this made it challenging to examine the effects of changing the Li content or Co content within the sheet. The standard dipole correction was applied;^[63] it eliminated spurious coupling between periodic images in the z-direction.

To go beyond metastable structures and to systematically examine the effect of the overall charge state (i.e., degree of delithiation), we found it necessary to also apply dynamic AIMD simulations in liquid water environments. Otherwise, the energy changes became very sensitive to the locations of the

OH^- in static DFT calculations. In dynamic AIMD simulations, TMA ions were omitted to reduce the inherently higher AIMD computational cost. AIMD simulation cells all had dimensions of $15.19 \times 11.50 \times 20 \text{ \AA}^3$. The number of H_2O molecules in the water-filled cell was determined as follows. Classical force field-based grand canonical Monte Carlo (GCMC)^[64] simulations were first applied to determine the average number of water molecules in the cell. The SPC/E water model^[65] and generic Lennard-Jones (LJ) force fields for the oxide sheet were adopted for this purpose, only. (Co, Ni, and Mn have LJ parameters $\epsilon = 1.841 \times 10^{-6} \text{ kJ mol}^{-1}$, $\sigma = 3.302 \text{ \AA}$; Li has $\epsilon = 0.6904 \text{ kJ mol}^{-1}$, $\sigma = 1.508 \text{ \AA}$; and O has $\epsilon = 0.6502 \text{ kJ mol}^{-1}$, $\sigma = 3.166 \text{ \AA}$.) Substrate atoms (including adsorbed OH^-) were frozen in water-free, DFT-optimized positions in GCMC calculations; only water molecules were inserted into/removed from the simulation cell and allowed to translate and rotate therein. From the last GCMC configuration, AIMD simulations were initiated. Two nanosheet stoichiometries, $\text{Li}_{10}\text{M}_{24}\text{O}_{48}$ and $\text{Li}_{14}\text{M}_{24}\text{O}_{48}$, were considered, with M = Ni or Co. Also included in the cells were 4 OH^- counterions (same as in the static calculations) and 94 H_2O molecules, as was one extra Co or Ni cation to be inserted into LCO or LNO sheets, respectively. We observed that the Co and Ni charge/spin states inside the nanosheet, including those not involved in cation exchange, can spontaneously change over the AIMD trajectory. When restarting an AIMD trajectory without pregenerated Kohn-Sham orbitals, for example after a trajectory has unexpectedly "crashed," we imposed both the global and local spin states from the last atomic configuration previously generated, saved the Kohn-Sham orbitals, and reinitiated AIMD with these orbitals without constraint on the total magnetic moment.

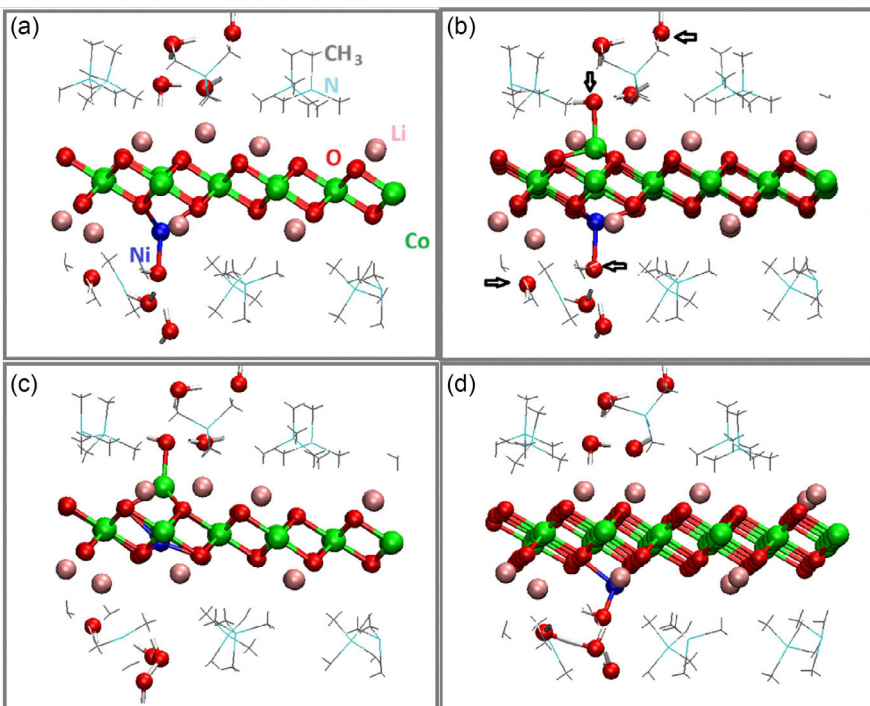


Figure 2. Configurations associated with $\text{Ni} \rightarrow \text{Co}$ exchange in the nanosheet in $\text{Li}_{10}\text{Co}_{24}\text{O}_{48} + \text{Ni}$. a) Ni-out ($\Delta E = 0.00 \text{ eV}$); b) both-out ($\Delta E = +0.26 \text{ eV}$), with key OH^- marked by arrows; c) Co-out ($\Delta E = -0.16 \text{ eV}$); and d) similar to (a) but with Ni displaced to a nearby adsorption site ($\Delta E = -0.08 \text{ eV}$). Pink, green, blue, red, gray, cyan, and white represent Li, Co, Ni, O, C, N, and H atoms, respectively.

AIMD free energy changes associated with $\text{Co} \leftrightarrow \text{Ni}$ replacement were computed using the potential of mean force (PMF) method via umbrella sampling.^[66,67] We first defined a 1D reaction coordinate given by

$$R = z_M - \sum_i \frac{z(O_i)}{3} \quad (1)$$

where z_M was the z-coordinate of the Ni or Co atom being inserted into the sheet, and $z(O_i)$ was the z-coordinate of one of the three O-anions in the nanosheet coordinated to M . A harmonic constraint of the form $A(R - R_o)^2$ was imposed on this coordinate, such that a series of R_o values forced the system to traverse the M -diffusion path. A was either 2 or 3 eV Å⁻². The effects of the constraints were analytically removed from the probability profile $P(R)$ at different values of R . The PMF, or $\Delta W(R)$, was obtained via

$$\Delta W(R) = -[k_B T \log P(R)] \quad (2)$$

k_B being the Boltzmann constant. In practice, the R values were discretized into 0.04 Å-sized bins. The trajectory length for each window characterized by R_o was 18–20 ps. See **Table 1** for details of the PMF sampling windows.

Operationally, the free energy associated with a local minimum “ a ” in the $\Delta W(R)$ profile was

$$G_a = -k_B T \log \sum_{R_1 < R_i < R_2} e^{\left(\frac{-\Delta W(R_i)}{k_B T}\right)} \quad (3)$$

with “ i ” labeling the bin at distance R_i and $R_1 \leq R_i \leq R_2$ delimiting the local minimum “ a ” which could be the initial or final state. We approximated the $\Delta W(R)$ computed at $T = 400$ K for use at $T = 300$ K in Equation (3). G_a so defined was actually missing logarithmic volumetric additive factors which however cancelled in the final property of interest, namely, the reaction free energy between two states, $\Delta G = G_b - G_a$. AIMD statistical uncertainties

were estimated by splitting the trajectory in each window into three equal parts, calculating $\Delta W(R_b) - \Delta W(R_a)$ where R_a and R_b were the limiting R values of each window, calculating the standard deviations, and propagating them by assuming Gaussian statistics. For the reaction barrier, the $\Delta W(R_i)$ value at the maximum of the PMF profile was imposed for the purpose of referencing to Equation (3).

At one end-point of the AIMD series of umbrella sampling windows sorted by the progression of R_o values, an adsorbed Ni^{2+} was coordinated to a H_2O molecule. At the other end point, the same cation was inside the nanosheet, coordinated to 6 O^{2-} anions in the sheet, and was no longer bound to any H_2O molecules. In the transition state (“barrier”) region intervening between these two points, interchange between these two types of configurations must occur. This required that a H_2O molecule reversibly formed and broke its coordination to Ni^{2+} . ($P(R)$) would have to exhibit higher probabilities at both end points than the middle of the transition state sampling window.) Therefore, significant diffusion motion of at least one unconstrained H_2O molecule was needed. This would usually necessitate longer trajectories. The 1D “ R ” reaction coordinate and PMF procedure discussed above proved insufficient to yield turning points in $P(R)$ within 20 ps trajectories with the several A and R_o choices we tried for the two simulation cells with 14 Li atoms. Instead, R probabilities saturated at one or the other of the window edges, indicating that the system was trapped in either the state with Co outside of the sheet (i.e., Ni inside) or both cations outside (i.e., Ni-outside) within the AIMD trajectory length. One solution would be to use metadynamics with 2D reaction coordinates and a metal–water coordination number constraint.^[68] However, it would take significant effort to convert coordination numbers to Cartesian coordinates needed to integrate the PMF into a ΔG (Equation (3)); we were unaware such a conversion was successfully conducted in 2D AIMD PMF studies in the literature. Here, we continued to use 1D umbrella sampling, but applied

Table 1. Details of AIMD/PMF sampling windows.

Figure	A	R_o	R_a	R_b	t_{all}	Figure	A	R_o	R_a	R_b	$t_{\text{al}}^{\text{a)}$
5a	0.0	NA	-0.68	-0.40	38.1	5a	3.0	-0.20	-0.40	-0.16	18.9
5a	2.0	0.00	-0.16	-0.00	21.0	5a	3.0	0.15	0.00	0.12	19.4
5a	3.0	0.20	0.12	0.40	20.6	5a	2.0	0.30	0.40	0.56	22.3
5a	2.0	0.60	0.56	0.72	19.7	5a	0.0	NA	0.72	1.12	19.7
5b	0.0	NA	-0.80	-0.32	19.9	5b	2.0	-0.10	-0.40	-0.16	19.2
5b	2.0	0.20	-0.16	0.16	21.0	5b	2.0	0.55	0.48	0.60	19.1
5b*	3.0	0.30	0.16	0.48	20.9	5b	0.0	NA	0.60	0.84	20.1
5c	2.0	NA	-0.84	-0.28	18.3	5c	2.0	0.00	-0.28	-0.12	27.7
5c	3.0	0.15	-0.12	0.32	20.5	5c	2.0	0.30	0.32	0.76	19.7
5c	0.0	NA	0.76	1.04	19.9						
5d	0.0	NA	-0.80	-0.36	18.1	5d	2.0	-0.10	-0.36	-0.12	21.8
5d	3.0	0.10	-0.12	0.04	21.2	5d	2.0	0.30	0.44	0.60	20.0
5d	2.0	0.65	0.60	0.76	20.5	5d	3.0	0.35	0.04	0.24	19.1
5d*	3.0	0.35	0.24	0.44	35.5						

^{a)} A (in eV) and R_o (Å) are parameters in the PMF harmonic potential described in the text; R_a and R_b are the limits of R used in each window; and t_{all} is the trajectory length in that window. An asterisk means an additional harmonic potential is added (see text).

an additional constraining potential only in the window expected to yield a barrier. The new potential took the form $B(R' - R'_0)^2$, where R' was the distance between the entering Ni^{2+} , and the oxygen atom of the H_2O molecule coordinated to Ni^{2+} . $B = 2.0 \text{ eV } \text{\AA}^{-2}$ and $R'_0 = 3.0 \text{ \AA}$. This forced one particular H_2O molecule to be partially coordinated to the transition metal cation. We stress that this potential was applied only in two barrier windows for AIMD simulation cells with 14 Li atoms.

3. Results and Discussion

3.1. Static DFT

Figure 2 depicts relevant configurations of the $\text{Li}_x\text{Co}_{24}\text{O}_{48}$ (LCO) sheet coated with a TMA monolayer as a Co cation inside the nanosheet is replaced by Ni ion from the solution environment. A complete monolayer in this surface cell appears to be formed with six TMA units without excessive steric interference from each other (not shown). In Figure 2b, one TMA is removed to accommodate two H_2O molecules and two OH^- (black arrows) on each surface. Nucleophilic species such as H_2O and OH^- are needed to coordinate to and stabilize the Ni^{2+} entering the nanosheet as well as the Co^{2+} exiting on the other side. In previous relevant LCO and NMC exfoliation experiments,^[39,40] a slightly alkaline aqueous media is present, suggesting the presence of H_2O and OH^- in the vicinity of the nanosheets. Therefore our model (Figure 2) is broadly consistent with experimental conditions. However, the surface density of TMA on exfoliated LCO surfaces has not been measured experimentally.

The relative energies associated with the configurations where the Ni cation is outside of the nanosheet ("Ni-out," Figure 2a), the Co cation is outside ("Co-out," Figure 2c), and the intermediate with both ions outside of the sheet ("both-out," Figure 2b) are given in the caption (see also Table 2). These energy changes are within 0.42 eV of each other. We use the starting point of the reaction, with Co inside the nanosheet and Ni outside (Ni-out), as the reference state. The intermediate state is 0.26 eV less favorable than this

reference, while the end point for the cation exchange (Co-out) is -0.16 eV more favorable. As Ni^{2+} is inserted into the sheet, its charge state remains unchanged, while the exiting Co cation turns from a Co^{3+} or Co^{4+} to Co^{2+} , spontaneously taking up excess electron(s) from the nanosheet in the process. At the same time, the initial ionic coordination between the Ni^{2+} and the $\text{H}_2\text{O}/\text{OH}^-$ group is broken, while the exiting Co^{2+} becomes coordinated to a H_2O molecule on the other side of the sheet. We stress that the initial atomic configuration, especially the position of the water/hydroxide bridge, must be prearranged to permit these configuration changes. In practice, starting with two transition metal cations outside of the nanosheet (the "both-out" configuration, Figure 2b) permits cation coordination on both sides of the sheet. Then, Figure 2a,c shows generated by manually displacing the Co and Ni, respectively, from Figure 2b.

The barriers (ΔE^*) from Figure 2a (Ni-out) to Figure 2b (both-out) and from Figure 2b (both-out) to Figure 2c (Co-out) are modest: 0.47 eV relative to Figure 2a, and 0.07 eV relative to Figure 2b (i.e., 0.33 eV relative to Figure 2a), respectively. These ΔE^* are similar to those predicted for the extrusion of six-coordinated Mn in the top transition metal layer of the basal plane of NMC oxides to four-coordinated sites on the outer surface.^[48] At room temperature, such ΔE^* can be surmounted in microseconds if we assume a standard unimolecular kinetic prefactor of $10^{12}/\text{s}$. Although the DFT method used does not have chemical accuracy, even a 0.2 eV DFT uncertainty in ΔE^* would not qualitatively change our conclusion that both steps of the Ni/Co cation exchange can take place within seconds or less.

One objection to the above calculations might be that both the Ni and the exiting Co are coordinated to the same three oxygen anions within the sheet. Inside bulk oxide environments, this is not an energetically favorable configuration. In Figure 2d, the displacement of the Ni^{2+} outside the sheet to a neighboring surface site, no longer bonded to the same three oxygen anions as the exiting Co, is examined. The predicted energy change of $\Delta E = -0.08 \text{ eV}$ is small and is reasonably close to that of Figure 2a ($\Delta E = 0.00 \text{ eV}$), showing that the initial Ni^{2+} placement on the nanosheet does not strongly affect the energies predicted.

Table 2. Relative energies or free energies in eV, as the type of calculation and stoichiometry vary.

Type	Detail	Figure	Ni-out	Both-out	Co-out ^{a)}
DFT-Ni	Bottom	2	0.00	+0.26 (0.47)	-0.16 (0.33)
DFT-Ni	Top	3	0.00	+0.28 (0.43)	+0.27 (0.51)
DFT-Ni	Mean	NA	0.00	+0.27 (0.45)	+0.06 (0.42)
DFT-Mn	Bottom	6	0.00	+0.15 (0.42)	-0.26 (0.33)
DFT-Mn	Top	NA	0.00	+0.14 (0.24)	-0.12 (0.28)
DFT-Mn	Mean	NA	0.00	+0.15 (0.33)	-0.19 (0.29)
AIMD	$\text{Li}_{20}\text{Co}_{24}\text{O}_{48}-\text{Ni}$	5a	NA	0.00 +/- 0.03	-0.02 (0.33)
AIMD	$\text{Li}_{14}\text{Co}_{24}\text{O}_{48}-\text{Ni}$	5b	NA	0.00 +/- 0.04	+0.32 (0.49)
AIMD	$\text{Li}_{20}\text{Ni}_{24}\text{O}_{48}-\text{Co}$	5c	NA	0.00 +/- 0.02	-0.15 (0.28)
AIMD	$\text{Li}_{14}\text{Ni}_{24}\text{O}_{48}-\text{Co}$	5d	NA	0.00 +/- 0.05	+0.37 (0.64)

^{a)}Static DFT calculations either feature Ni- or Mn-insertion. AIMD (PMF) simulations are assumed not to have top- or bottom-side Ni adsorption dependences because they feature equilibrium sampling at finite temperature. Values in brackets are reaction barriers measured from the reference ("0.00"). AIMD ΔG statistical uncertainties are denoted by "+/-".

The top and bottom sides of the static simulation cell are not symmetric, and it is useful to see how the predicted energies depend on that asymmetry. Thus, the same nanosheet is re-examined with the positions of the Ni^{2+} and the exiting Co switched (**Figure 3**), so the top and bottom sides are reversed. We find that the relative energy ΔE of the intermediate (0.28 eV, **Figure 3b**) is similar to that seen in the intermediate state in **Figure 2b** (both-out). The Co-out configuration (**Figure 3c**) has a higher energy of $\Delta E = 0.27 \text{ eV}$, which is within 0.43 eV of **Figure 2c** but is clearly different. The barriers associated with the two steps are $\Delta E^* = 0.51 \text{ eV}$ and $\Delta E^* = 0.43 \text{ eV}$ relative to **Figure 3a** (in the second step, $\Delta E^* = 0.16 \text{ eV}$ from the intermediate of **Figure 3b**). Table 2 also reports the mean energy changes after averaging those of **Figure 2** and **3**.

Overall, these calculations suggest that the predicted ΔE and ΔE^* values do not strongly depend on the local configuration in static DFT calculations. However, an inherent uncertainty of $\approx 0.3 \text{ eV}$, found when switching Ni and Co, seems to persist in static DFT calculations, likely due to the system being trapped in metastable structures. For this reason, it proves challenging to use static DFT calculations to examine the effect of changing the number of Li atoms to mimic the nanosheet state of charge, or varying the number of Co atoms (replaced by Ni) to mimic the state of cation exchange.

3.2. AIMD

This section focuses on AIMD simulations in aqueous environments. With molecular dynamics-based sampling of local configurations, the metastable structure ambiguity of static DFT

calculations should be avoided. Both $\text{Li}_n\text{Co}_{24}\text{O}_{48} + \text{Ni}$ and $\text{Li}_n\text{Ni}_{24}\text{O}_{48} + \text{Co}$ are considered; n can be either 20 or 14. In effect, ten of the Li^+ ions present electrostatically replace the 10 TMA monovalent cations in the static DFT calculations. Hence $n = 20$ has the same charge state as **Figure 2** and **3** (3.33 for each transition metal ion on average), and $n = 14$ is associated with a slightly higher charge state (+3.58 on average). The $\text{Co}_{24}\text{O}_{48}$ nanosheets mimic the initial stage of cation exchange while the $\text{Ni}_{24}\text{O}_{48}$ sheets represent the end stage. Due to the cost and complexity of AIMD-PMF simulations, we only consider half of the replacement step, namely from “both-out” to “Co-out;” in the latter case, Ni is inside the sheet.

Figure 4a,b shows the both-out and Co-out configurations for $\text{Li}_{20}\text{Co}_{24}\text{O}_{48} + \text{Ni}$. One advantage of AIMD simulations with a bulk water-like environment, immediately evident in these snapshots, is that as Ni^{2+} and Co^{2+} exit the nanosheet, a network of H_2O and/or OH^- is available to coordinate to them, unlike in static DFT calculations where such molecules/anions must be initially put in place. Furthermore, the protonation states of $\text{H}_2\text{O}/\text{OH}^-$ adsorbed on the nanosheet surfaces can spontaneously change during the finite-temperature dynamic trajectory to reflect the equilibrium proton distribution.

Figure 5a depicts the PMF profile ($\Delta W(R)$) as the Ni-insertion coordinate R varies. Note that the absolute value of $\Delta W(R)$ is arbitrary, and the left-most minimum is shifted to appear at 0.0 eV. Unlike in static DFT calculations (**Figure 2b,c**), in which Co outside the nanosheet (Co-out) is more favorable than having both Co and Ni outside (both-out) by 0.42 eV, Ni insertion is almost isothermal. Upon numerical integration of the two local minima in $\Delta W(R)$ (**Equation (3)**), we find $\Delta G = -0.02 \text{ eV}$. The difference

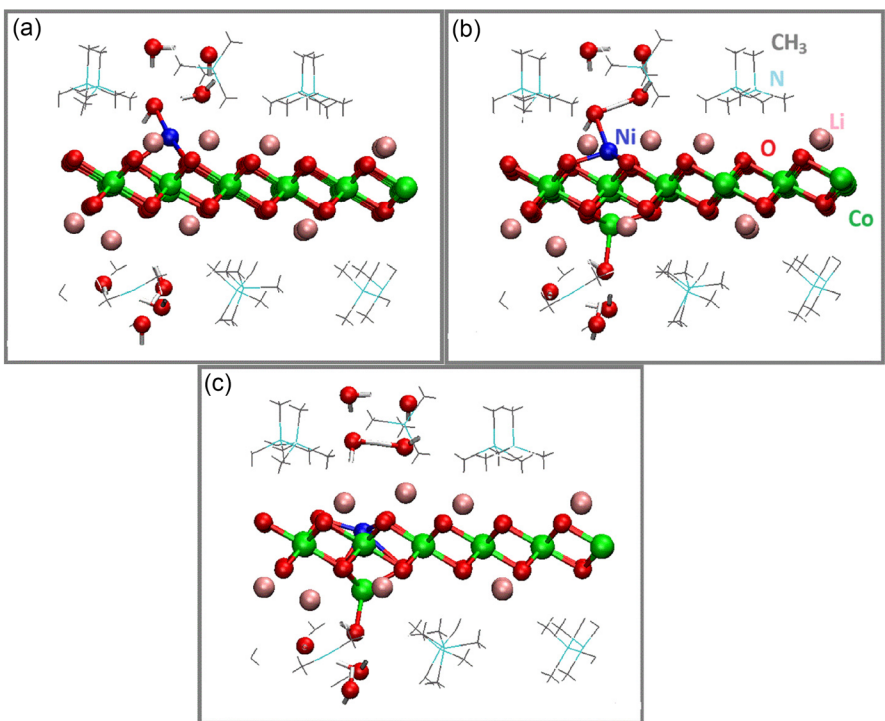


Figure 3. Similar to **Figure 2**, but with the initial positions of the Ni and the exiting Co reversed. a) Ni-out ($\Delta E = 0.00 \text{ eV}$); b) both-out ($\Delta E = 0.28 \text{ eV}$); c) Co-out ($\Delta E = 0.27 \text{ eV}$).

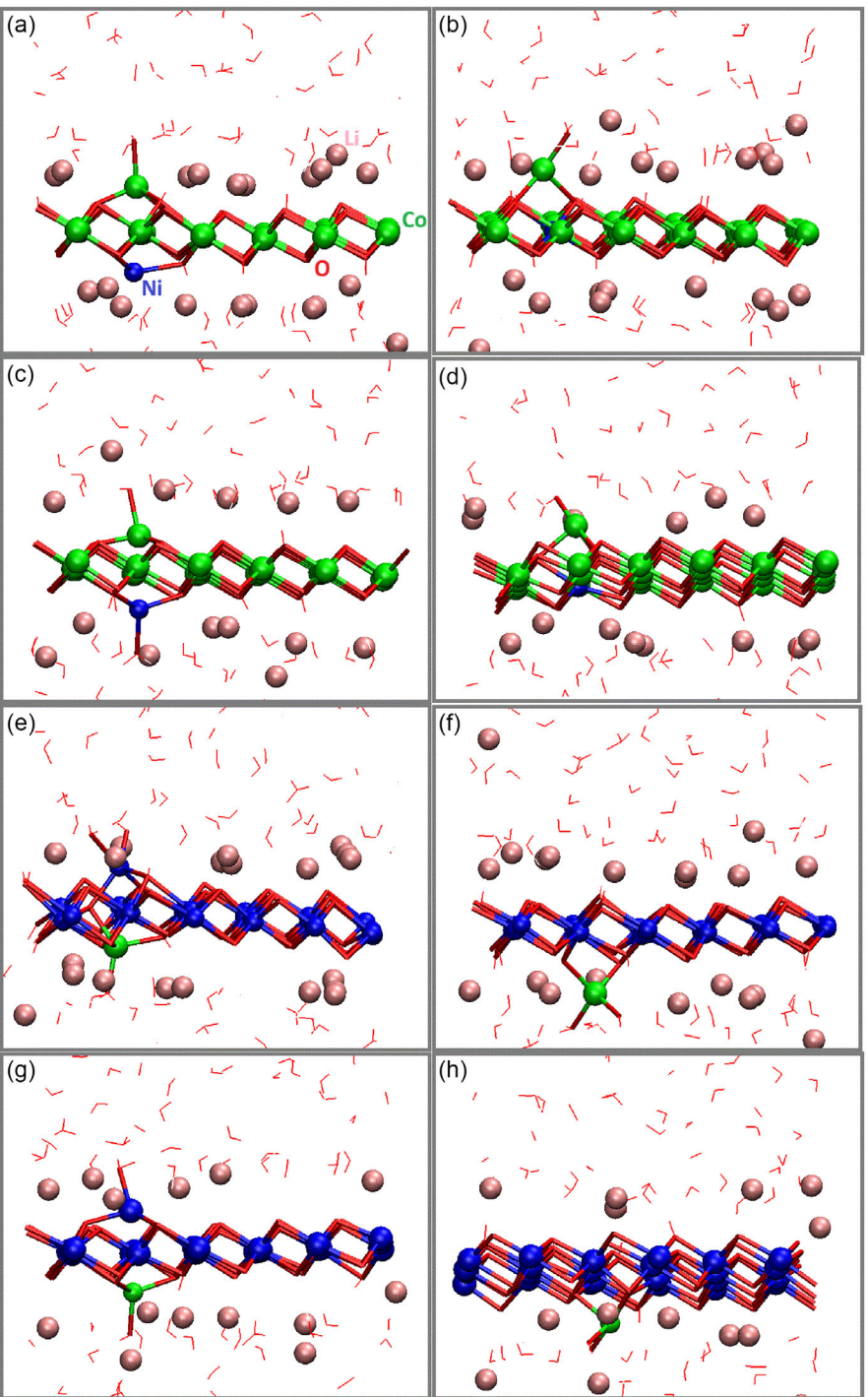


Figure 4. AIMD snapshots of both-out/Co-out (before/after Ni insertion) configurations for: a,b) $\text{Li}_{20}\text{Co}_{24}\text{O}_{48}$; c,d) $\text{Li}_{14}\text{Co}_{24}\text{O}_{48}$; e,f) $\text{Li}_{20}\text{Ni}_{24}\text{O}_{48}$; g,h) $\text{Li}_{14}\text{Ni}_{24}\text{O}_{48}$. Pink, green, blue, red, gray, and white represent Li, Co, Ni, O, C, and H atoms, respectively. H_2O and OH^- are depicted as thin lines or rods.

between the ΔE in Figure 2b,c and ΔG in Figure 5a may be due to better sampling of the aqueous environment and/or the absence of TMA in the AIMD model. Qualitatively speaking, we conjecture that the magnitude of ΔG associated with Ni^{2+} insertion is small, and its sign and magnitude may be environment dependent; the presence of TMA may affect the results. The free energy barrier also remains small, at $\Delta G^* = 0.33 \text{ eV}$ compared with the static $\Delta E^* = 0.33 \text{ eV}$ value (Figure 2). Both values suggest the

reaction step can take place within milliseconds at room temperature. Note that the $\Delta W(R)$ profile is asymmetric. The potential well is broader in the both-out configuration, where there is more favorable vibrational entropy. In the Co-outside configuration, the Ni^{2+} coordinated to 6 O^{2-} anions inside the nanosheet is more spatially constrained there.

Figure 5b depicts the PMF associated with the transition between both-out (Figure 4c) and Co-out (Figure 4d) for a

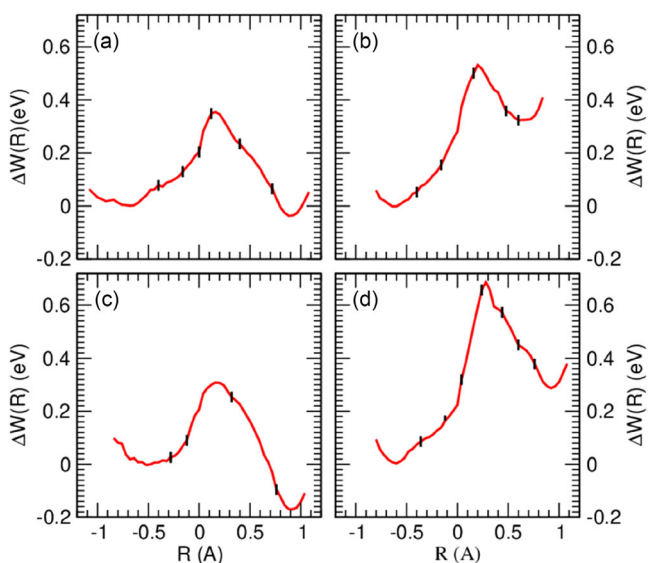


Figure 5. $\Delta W(R)$ as functions of reaction coordinate R (see text). Panels a–d) are associated with Figure 4a,b, Figure 4c,d, Figure 4e,f, and Figure 4g,h, respectively. Black vertical lines show the limiting R values used in each sampling window.

nanosheet with decreased Li content ($\text{Li}_{14}\text{Co}_{24}\text{O}_{48}$). $\Delta G = 0.32$ eV is higher than that for Figure 5a by 0.34 eV, while $\Delta G^* = 0.49$ eV is higher by 0.16 eV. This suggests that decreasing the Li content makes Ni replacement of Co in the nanosheet less energetically and kinetically favorable, albeit by a small fraction of an eV.

This Li content trend is also observed when we switch to the $\text{Li}_n\text{Ni}_{24}\text{O}_{48} + \text{Co}^{2+}$ system, with $n = 14$ and 20. The PMF in Figure 5c is associated with the transition between both-out

(Figure 4e) and Co-out (Figure 4f) configurations for $n = 20$, while Figure 5d is associated with the transition between Figure 4g,h for $n = 14$. ΔG increases from -0.15 eV for $n = 20$ to $+0.37$ eV for $n = 14$, while ΔG^* increases from 0.28 to 0.64 eV. Overall, the effect of higher Ni content inside the sheet, compared with Figure 5a,b, is to make Ni insertion more thermodynamically favorable at the higher Li-content, while there is less ΔG difference at the lower Li content. Although the barrier $\Delta G^* = 0.64$ eV becomes less favorable at lower Li content, it is still consistent with subsecond cation exchange rates. Comparing with Figure 5a,c suggests that the initial insertion of Ni to replace Co may be a thermodynamic bottleneck at high Li content; the process is expected to be more energetically favorable as cation exchange proceeds. Decrease of the Li content in nanosheets (i.e., increasing the oxidation state) makes the cation exchange less favorable (Figure 5b,d). We note, however, that delithiation facilitates exfoliation (Figure 1).^[39,40] There may be an optimal Li content at which the trade-off between the two processes is optimized.

EV batteries with layered oxides as cathode materials comprise NMC111, 532, 622, and 811 instead of LiCoO_2 . For this reason, Mn also needs to be considered. We have briefly examined Mn^{2+} exchanging for Co in Li_xCoO_2 using static DFT calculations (Figure 6), akin to those in Figure 2. The initial configurations in these Mn calculations are taken from the optimized configurations of the LCO + Ni sheet (Figure 2). The predictions are similar to those for Figure 2a–c. The ΔE values are within 0.1 eV of the Ni-insertion cases. The ΔE^* values are slightly smaller than for Ni in Figure 2 and are 0.42 and 0.33 eV, respectively. This suggests that $\text{Mn} \rightarrow \text{Co}$ cation exchange should occur as readily as $\text{Ni} \rightarrow \text{Co}$ exchange. On the opposite surface (not shown but akin to Figure 3; see Table 2), the Mn-out, both-out, and Co-out

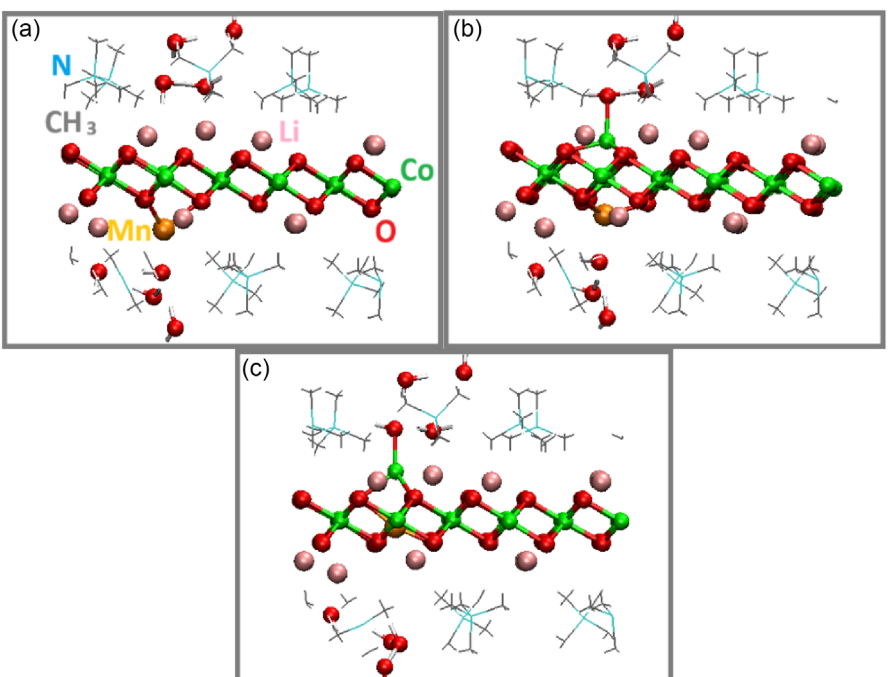


Figure 6. Configurations associated with $\text{Mn} \rightarrow \text{Co}$ exchange in the nanosheet in $\text{Li}_{10}\text{Co}_{24}\text{O}_{48} + \text{Mn}$. a) Mn outside ($\Delta E = 0.00$ eV); b) both Mn and Co outside ($\Delta E = +0.15$ V); and c) Co outside ($\Delta E = -0.26$ eV). Pink, green, orange, red, gray, cyan, and white represent Li, Co, Mn, O, C, N, and H atoms, respectively.

configurations are 0.00, 0.15, and -0.12 eV, while the ΔE^* for the two steps are 0.24 and 0.28 eV referenced to Mn-out. Again, the predictions are qualitatively similar to those in Figure 3.

3.3. Discussions

This work is a basic science demonstration and is not intended to prescribe an economically viable recipe for battery recycling. A “lean solvent” approach to the cation exchange proposed herein is needed to reduce chemical waste. Postexchange separation of transition metal cations in the aqueous waste stream is necessary,^[69] although that is also true of acid leaching processes used currently.^[2,3] We propose that there may be other advantages in exfoliation-based recycling approaches. For example, if the cation exchange route proves too challenging (e.g., in terms of producing a uniform cation distribution and high-Ni stoichiometry), exfoliation may be a useful intermediate step to promote lower-temperature acid leaching. Exchange of inexpensive, redox-inactive metal ions like Mg^{2+} and Al^{3+} for transition metal ions in exfoliated NMC nanosheets, with the oxide discarded afterwards, is another possibility.

This DFT work is not suited to determining the rate of transition metal recovery. Given the relatively low reaction barriers predicted in this work, it is likely the kinetic bottleneck lies elsewhere. Another possibility is that the limiting factors are now thermodynamics (e.g., adding enough Ni^{2+} in solution to shift the predicted, slightly unfavorable Ni insertion equilibrium constant to more favorable values).

Upcycling “Ni-lean” precursors such as NMC111 into “Ni-rich” materials is an active area of research, with recent reports describing ball milling/sintering and molten salt-based methods for converting polycrystalline NMC111 into single-crystalline NMC811 and 622 with improved electrochemical performance.^[16,70] Much of the recent focus on upcycling has been on bulk and microscale materials. (While single crystals have attracted significant interest, there remain degradation issues at high voltages.^[71]) Corresponding research on nanoscale materials has not been reported, but use of exfoliated nanosheets could dramatically increase product tunability and uniformity of Ni distribution in polycrystalline NMCs.

In a broader context, exfoliation-based methods may be leveraged to achieve direct upcycling of spent, low-Ni cathode materials without relying on hydro- or pyrometallurgical processing. Synergistic, integrated experimental/theoretical studies can help construct such a strategy around nanoscale manipulations by addressing the impacts of bulk-to-nanosheet conversion processes, such as structural and compositional changes like lattice vacancy formation and the alteration of cobalt and oxygen valence states.^[72] Understanding cycling-induced phase changes due to Li^{+} deficiency and migration of Ni^{2+} between layers will benefit NMC upcycling strategies, which can be more challenging than LCO due to the more complex chemistry of NMC.^[73]

Improved synthesis methods are also important to developing exfoliation-based cathode recycling and cation exchange-based upcycling routes. One impactful area for exploration is determining the optimal Li^{+} content for maximizing both

exfoliation, which generates higher yields of fully exfoliated monolayer nanosheets at low Li^{+} concentrations, and cation exchange, which benefits from high Li^{+} concentrations that increase the oxidation state of the nanosheets. Highly controlled delithiation methods, such as the electrochemical delithiation route previously reported by the Chan group, will greatly facilitate these investigations.^[39,40] Improved acid delithiation routes,^[74] adapted from topochemical manipulation of layered perovskites, extract more Li^{+} and may avoid the irreversible proton binding that degrades electrochemical activity after conventional acid treatment.

Improving exfoliation quality to generate monolayer nanosheets is also important for achieving precise stoichiometric control by maximizing available surface exchange sites and facilitating cation mobility within the materials. Current promising pathways exploit improved heating methods, such as hydrothermal and microwave reactors, and manipulate experimental parameters such as pH and the alkyl moiety in the quaternary ammonium compound used to facilitate exfoliation. Understanding the underlying exfoliation mechanisms may expand the range of suitable spent cathode materials beyond LCO and NMC111, as current exfoliation techniques have limited success with Ni-rich compounds such as NMC811, 523, and 622.^[40] Flexibility to treat a wide variation of spent cathode materials is critical within real battery waste streams.

Looking forward, overcoming the thermodynamic barrier associated with Ni insertion at low Li content could provide a framework for selecting full incorporation of substituent cations into host lattice (“oxidative incorporation”) instead of energetically favorable “intercalative restacking,” in which negatively charged nanosheets restack around surface layers of substituent cations, a persistent hindrance to viable upcycling methods.^[34] In terms of computational studies, DFT results can improve and expand current machine learning (ML) models specifically for cation exchange, which can then aid determination of optimal experimental conditions. For example, the dynamic AIMD free energy calculations applied herein are computationally costly to implement. ML force fields trained by AIMD and/or static DFT calculations may represent a future pathway toward faster cation exchange calculations.

4. Conclusion

We have applied static DFT and finite-temperature AIMD PMF calculations to examine the energetics and kinetics of cation exchange in exfoliated Li_xCoO_2 nanosheets in aqueous media, coated with bulky organic tetramethylammonium (TMA) cations or otherwise. We focus on the first two steps in the Ni^{2+} exchange with the Co cation. The first involves Co removal from within the nanosheet, becoming adsorbed on to the nanosheet surface and forming a configuration with “both cations outside” of the nanosheet. The second, subsequent step is the insertion of a Ni^{2+} adsorbed outside the nanosheet into the Co vacancy.

The (free) energy barriers for these two steps in the nanosheet are below 0.7 eV in all cases considered, suggesting subsequent cation exchange kinetics. This is noteworthy because the

corresponding process in bulk, 3D NMC, namely the diffusion of Co^{3+} from the transition metal layers to the interlayer space via the precursor to the “dumbbell” defect, is high and usually unsurmountable within laboratory time scales at room temperature.

Static DFT and dynamic AIMD free energy calculations are in qualitative agreement. Focusing on the AIMD simulations, which can more reliably generate predictive trends, we find that the cation exchange becomes less favorable at higher nanosheet oxidation states. This suggests that cation exchange is favored under mild oxidation (i.e., delithiation) conditions. However, substantial oxidation is needed for exfoliation.^[39,40] This means that an optimal state of charge should be determined that can benefit both exfoliation and subsequent cation exchange. At high Li content, the free energies associated cation exchange become more favorable as the amount of Ni in the nanosheet increases. In other words, the beginning stage of cation exchange (mostly Li_xCoO_2) is less favorable than the end stage (mostly Li_xNiO_2). This suggests that the initial stage may be a slight bottleneck. A different trend is found at low Li content; the kinetic barrier for cation exchange is higher at larger Ni content. Nevertheless, even the most unfavorable ΔE or ΔG predicted is modest in magnitude ($+0.35$ eV). Overall, this suggests the oxidation state at which nanosheet exfoliation occurs can alter and help optimize the cation exchange process. We also conjecture that the electrolyte environment can change the energetics and will examine this via further modeling work in the future. While there is uncertainty in each type of calculation, the DFT and AIMD findings presented herein will provide guidelines for future improvement of transition metal cation exchange in exfoliated NMC and layered transition metal oxide nanosheets.

Acknowledgements

The authors thank Anastasia Ilgen, Kirsten D. Jones, Boyoung Song, Bryan R. Wygant, Katharine Harrison, and Fang Liu for useful discussions. This article has been authored by an employee of National Technology & Engineering Solutions of Sandia, LLC, under contract no. DE-NA0003525 with the U.S. Department of Energy (DOE). The employee owns all rights, titles, and interests in and to the article and is solely responsible for its contents. The United States Government retains and the publisher, by accepting the article for publication, acknowledges that the United States Government retains a nonexclusive, paid-up, irrevocable, worldwide license to publish or reproduce the published form of this article or allows others to do so, for United States Government purposes. The DOE will provide public access to these results of federally sponsored research in accordance with the DOE Public Access Plan <https://www.energy.gov/downloads/doe-public-access-plan>. This article describes objective technical results and analysis. Any subjective views or opinions that might be expressed in the article do not necessarily represent the views of the U.S. Department of Energy or the United States Government.

Conflict of Interest

The authors declare no conflict of interest.

Data Availability Statement

The data that support the findings of this study are available from the corresponding author upon reasonable request.

Keywords: ab initio molecular dynamics • battery recycling • density functional theory • free energy calculations • nickel–cobalt exchange

- [1] Z. J. Baum, R. E. Bird, X. Yu, J. Ma, *ACS Energy Lett.* **2022**, *7*, 712.
- [2] A. R. Shekhar, M. H. Parekh, V. G. Pol, *J. Power Sources* **2022**, *523*, 231015.
- [3] W. Yu, Y. Guo, S. Xu, Y. Yang, Y. Zhao, J. Zhang, *Energy Storage Mater.* **2023**, *54*, 172.
- [4] E. Mossali, N. Picone, L. Gentilini, O. Rodriguez, J. M. Perez, M. Colledani, *J. Environ. Manage.* **2020**, *264*, 110500.
- [5] F. Larouche, F. Tedjar, K. Amouzegar, G. Houlachi, P. Bouchard, G. P. Demopoulos, K. Zaghib, *Materials* **2020**, *13*, 801.
- [6] K. Kim, D. Raymond, R. Candeago, X. Su, *Nat. Commun.* **2021**, *12*, 6554.
- [7] X. Chang, M. Fan, C.-F. Gu, W.-H. He, Q. Meng, L.-J. Wan, Y.-G. Guo, *Angew. Chem. Int. Ed.* **2022**, *61*, e202202558.
- [8] Y. Shi, M. Zhang, Y. S. Meng, Z. Chen, *Adv. Energy Mater.* **2019**, *8*, 1900454.
- [9] X. Xiao, L. Wang, Y. Wu, Y. Song, Z. Chen, X. He, *Energy Environ. Sci.* **2023**, *16*, 2856.
- [10] P. Xu, Z. Yang, X. Yu, J. Holoubek, H. Gao, M. Li, G. Cai, I. Bloom, H. Liu, Y. Chen, K. An, K. Z. Pupek, P. Liu, Z. Chen, *ACS Sus. Chem. Engr.* **2021**, *9*, 4543.
- [11] H. Gao, D. Tran, Z. Chen, *Curr. Opin. Electrochem.* **2022**, *31*, 100875.
- [12] V. Gupta, X. Yu, H. Gao, C. Brooks, W. Li, Z. Chen, *Adv. Energy Mater.* **2023**, *13*, 2203093.
- [13] J. J. WangMa, J. Ma, Z. F. Zhuang, Z. Liang, K. Jia, G. J. Ji, G. M. Zhou, H. M. Cheng, *Chem. Rev.* **2024**, *124*, 2839.
- [14] C. Xing, M. Yao, L. Fei, *Energy Storage Mater.* **2024**, *71*, 103636.
- [15] Z. Z. Liu, H. M. Li, M. M. Han, L. Fang, Z. Fu, H. M. Zhang, G. Z. Wang, Y. X. Zhang, *Adv. Energy Mater.* **2023**, *13*, 2302058.
- [16] H. Gao, Q. Yan, D. Tran, X. Yu, H. Liu, M. Li, W. Li, J. Wu, W. Tang, V. Gupta, J. Luo, Z. Chen, *ACS Energy Lett.* **2023**, *8*, 4136.
- [17] X. Ma, J. Hou, P. Vanaphuli, Z. Yao, J. Fu, L. Azhari, Y. Liu, Y. Wang, *Chem* **2022**, *8*, 1944.
- [18] K. S. Kim, M. K. Jeon, S. H. Song, S. Hong, H. S. Kim, S. W. Kim, J. Kim, P. Oh, J. Hwang, J. Song, J. Ma, J.-J. Woo, H. Kim, *J. Mater. Chem. A* **2023**, *11*, 21222.
- [19] T. Wang, H. Luo, J. Fan, B. P. Thapaliya, Y. Bai, I. Belharouak, S. Dai, *iScience* **2022**, *25*, 103801.
- [20] K. Davis, G. P. Demopoulos, *Next Energy* **2024**, *4*, 100122.
- [21] <https://www.iea.org/reports/global-ev-outlook-2023/trends-in-batteries>.
- [22] I. Mufungizi, *Int. Geol. Rev.* **2024**, *66*, 754.
- [23] F. Xin, H. Zhou, X. Chen, M. Zuba, N. Chernova, G. Zhou, M. S. Whittingham, *ACS Appl. Mater. Interfaces* **2019**, *11*, 34889.
- [24] M. Yi, W. D. Li, A. Manthiram, *Chem. Mater.* **2022**, *34*, 629.
- [25] L. Hamitouche, C. Robert, A.-L. Rollet, V. Briois, M. Selmane, A. G. P. Gutierrez, S. Leclerc, D. Krulic, N. Fatouros, J. Sirieix-Planet, L. Michot, M.-L. Doublet, D. Dambourret, *Chem. Mater.* **2024**, *36*, 2544.
- [26] H. Zhang, Y. Ji, Y. Yao, L. Qie, Z. Cheng, Z. Ma, X. Qian, R. Yang, C. Li, Y. Guo, Y. Yuan, H. Xiao, H. Yang, J. Ma, Y. Huang, *Energy Environ. Sci.* **2023**, *16*, 2561.
- [27] Y. Zhang, N. Song, J. He, R. Chen, X. Li, *Nano Lett.* **2019**, *19*, 512.
- [28] B. J. Beberwyck, A. P. Alivisatos, *J. Am. Chem. Soc.* **2012**, *134*, 19977.
- [29] B. J. Beberwyck, Y. Surendranath, A. P. Alivisatos, *J. Phys. Chem. C* **2013**, *117*, 19759.
- [30] D. H. Son, S. M. Hughes, Y. Yin, A. P. Alivisatos, *Science* **2004**, *306*, 1009.
- [31] H. Li, M. Zanella, A. Genovese, M. Povia, A. Falqui, C. Giannini, L. Manna, *Nano Lett.* **2011**, *11*, 4964.
- [32] A. J. Friedrich, M. Helgeson, C. Liu, C. Wang, K. M. Rosso, M. M. Scherer, *Environ. Sci. Tech.* **2015**, *49*, 8479.
- [33] S. Lentijo-Mozo, D. Deiana, E. Sogne, A. Casu, A. Falqui, *Chem. Mater.* **2018**, *30*, 8099.
- [34] J. Lim, J. M. Lee, B. Park, X. Jin, S.-J. Hwang, *Nanoscale* **2017**, *9*, 792.
- [35] A. Liu, N. Zhang, J. Li, T. Casagrande, C. Butcher, J. Martinez, A. Korinek, G. Botton, J. R. Dahn, *J. Electrochem. Soc.* **2018**, *165*, A2781.
- [36] Q. Ma, B. Li, F. Huang, Q. Pang, Y. Chen, J. Z. Zhang, *Electrochim. Acta* **2019**, *317*, 684.

- [37] B. Xu, C. R. Fell, M. Chi, Y. S. Meng, *Energy Environ. Sci.* **2011**, *4*, 2223.
- [38] I. G. McKendry, A. C. Thenuwara, S. L. Shumlas, H. Peng, Y. V. Aulin, P. R. Chinnam, E. Borguet, D. R. Strongin, M. J. Zdilla, *Inorg. Chem.* **2018**, *57*, 557.
- [39] Q. Cheng, T. Yang, Y. Li, M. Li, C. K. Chan, *J. Mater. Chem. A* **2016**, *4*, 6902.
- [40] Q. Cheng, T. Yang, M. Li, C. K. Chan, *Langmuir* **2017**, *31*, 9271.
- [41] A. Basch, L. de Campo, J. H. Albering, J. W. White, *J. Solid State Chem.* **2014**, *220*, 102.
- [42] Y. Zhu, X. Luo, H. Zhi, X. Yang, L. Xing, Y. Liao, M. Xu, W. Li, *ACS Appl. Mater. Interfaces* **2017**, *9*, 12021.
- [43] K. Hua, X. Li, Z. Fu, D. Fang, R. Bao, J. Yi, Z. Luo, *J. Solid State Chem.* **2019**, *273*, 287.
- [44] J. Liang, R. Ma, N. Ivi, Y. Ebina, K. Takada, T. Sasaki, *Chem. Mater.* **2010**, *22*, 371.
- [45] R. Zhang, T. Averianov, R. Andris, M. J. Zachman, E. Pomerantseva, *J. Phys. Chem. C* **2023**, *127*, 919.
- [46] K. Pachuta, H. Volkova, B. Hirt, M.-H. Berger, E. Pentzer, A. Sehirioglu, *J. Am. Ceramic Soc.* **2022**, *105*, 1904.
- [47] O. C. Compton, A. Abouimrane, Z. An, M. J. Palmeri, L. C. Brinson, K. Amine, S. T. Nguyen, *Small* **2012**, *8*, 1110.
- [48] K. Leung, *Chem. Mater.* **2023**, *35*, 2518.
- [49] T. Li, X.-Z. Yuan, L. Zhang, D. Song, K. Shi, C. Bock, *Electrochem. Energy Rev.* **2020**, *3*, 43.
- [50] N. N. Intan, K. Klyukin, V. Alexandrov, *ACS Appl. Mater. Interfaces* **2019**, *11*, 20110.
- [51] J. W. Bennett, D. T. Jones, X. Huang, R. J. Hamers, S. E. Mason, *Environ. Sci. Tech.* **2018**, *52*, 5792.
- [52] J. W. Bennett, D. T. Jones, R. J. Hamers, S. E. Mason, *Inorg. Chem.* **2018**, *57*, 13300.
- [53] G. Kresse, J. Furthmuller, *Phys. Rev. B* **1996**, *54*, 11169.
- [54] G. Kresse, J. Furthmuller, *Comput. Mater. Sci.* **1996**, *6*, 15.
- [55] G. Kresse, D. Joubert, *Phys. Rev. B* **1999**, *59*, 1758.
- [56] J. Paier, M. Marsman, G. Kresse, *J. Chem. Phys.* **2007**, *127*, 024103.
- [57] J. P. Perdew, K. Burke, M. Ernzerhof, *Phys. Rev. Lett.* **1996**, *77*, 3865.
- [58] S. L. Dudarev, G. A. Botton, S. Y. Savrasov, C. J. Humphreys, A. P. Sutton, *Phys. Rev. B* **1998**, *57*, 1505.
- [59] D. Kramer, G. Ceder, *Chem. Mater.* **2009**, *21*, 3799.
- [60] S. Grimme, *J. Comput. Chem.* **2006**, *27*, 1787.
- [61] V. Kostal, P. E. Mason, H. Martinez-Seara, P. Jungwirth, *J. Phys. Chem. Lett.* **2023**, *14*, 4403.
- [62] G. Henkelman, B. P. Uberuaga, H. Jonsson, *J. Chem. Phys.* **2000**, *113*, 9901.
- [63] J. Neugebauer, M. Scheffler, *Phys. Rev. B* **1992**, *46*, 16067.
- [64] M. G. Martin, A. P. Thompson, *Fluid Phase Equil.* **2004**, *217*, 105.
- [65] H. J. C. Berendsen, J. R. Grigera, T. P. Straatsma, *J. Phys. Chem.* **1987**, *91*, 6269.
- [66] K. Leung, I. M. B. Nielsen, L. J. Criscienti, *J. Am. Chem. Soc.* **2009**, *131*, 18358.
- [67] K. Leung, L. J. Criscienti, A. W. Knight, A. G. Ilgen, T. A. Ho, J. A. Greathouse, *J. Phys. Chem. Lett.* **2018**, *9*, 5379.
- [68] S. Roy, M. D. Baer, C. J. Mundy, G. K. Schenter, *J. Chem. Theory Comput.* **2017**, *13*, 3470.
- [69] B. Song, R. E. Sikma, M. L. Meyerson, K. Leung, K. M. M. Sanchez, J. G. Smith, D. F. Sava Gallis, A. G. Ilgen, *Sep. Purif. Technol.* **2025**, *355*, 129379.
- [70] X. Ma, J. Hou, P. Vanaphuti, Z. Yao, J. Fu, L. Azhari, Y. Liu, Y. Wang, *Chem* **2022**, *8*, 1944.
- [71] W. Huang, T. Liu, L. Yu, J. Wang, T. Zhou, J. Liu, T. Li, R. Amine, X. Xiao, M. Ge, L. Ma, S. N. Ehrlich, M. V. Holt, J. Wen, K. Amine, *Science* **2024**, *384*, 912.
- [72] K. G. Pachuta, E. B. Pentzer, A. Sehirioglu, *J. Am. Ceramic Soc.* **2019**, *102*, 5603.
- [73] Y. Shi, G. Chen, F. Liu, X. J. Yue, Z. Chen, *ACS Energy Lett.* **2018**, *3*, 1683.
- [74] S. Akbarian-Tefaghi, T. Rostamzadeh, T. T. Brown, C. Davis-Wheeler, J. B. Wiley, *ChemNanoMat* **2017**, *3*, 538.

Manuscript received: December 24, 2024

Revised manuscript received: March 3, 2025

Version of record online: March 23, 2025